remote sensing

MDPI

Article

Experimental Investigation on Fragmentation Identification in Loose Slope Landslides by Infrared Emissivity Variability Features

Xiangxin Liu [1], Lixin Wu [2,*], Wenfei Mao [2] and Licheng Sun [2]

[1] School of Civil and Surveying and Mapping Engineering, Jiangxi University of Science and Technology, Ganzhou 341000, China; liuxx@jxust.edu.cn
[2] School of Geosciences and Info-Physics, Central South University, Changsha 410083, China; maowenfei@csu.edu.cn (W.M.); slcheng@csu.edu.cn (L.S.)
* Correspondence: wulx66@csu.edu.cn

Abstract: Infrared radiation (IR) features that are influenced by infrared emissivity ε and physical temperature T_d have been successfully applied to the early-warning of landslides. Although the infrared emissivity of a rock is a key parameter to determine its thermal radiation properties, the effect of particle size on the infrared emissivity of rock fragments is unknown. So in this paper, granite, marble, and sandstone were used as examples to conduct infrared imaging experiments on rock fragments. Their equivalent emissivity was used to interpret the detected infrared emission, including that from indoor backgrounds. In addition, the characteristics of changes in equivalent emissivity were discussed with reference to changes in observation direction and zenith angle. Then, a computation model of equivalent emissivity based on multiple observation directions and zenith angles was built to reveal the change in equivalent emissivity with particle sizes. The result indicates that the indoor background radiation has a predominant direction just above the rock fragments. The maximum deviation of infrared brightness temperature (IBT) was 0.260 K, and the maximum deviation of equivalent emissivity among different observation directions and zenith angles was 0.0065. After eliminating the influence of directional and angle effects with the operation of normalization, the general law of equivalent emissivity for all rock fragments that change with particle size is consistent. The maximum equivalent emissivity occurs at particle size 5 mm in the condition of particle size larger than 1 mm, while the equivalent emissivity changes inversely with particle size in the condition of particle size smaller than 1 mm. Above all, this study contributes new cognitions to Remote Sensing Rock Mechanics, and provides valuable evidence for better thermal infrared remote sensing monitoring on loose slope landslides.

Keywords: remote sensing rock mechanics; particle sizes; infrared brightness temperature; loose slope; equivalent emissivity

check for updates

Citation: Liu, X.; Wu, L.; Mao, W.; Sun, L. Experimental Investigation on Fragmentation Identification in Loose Slope Landslides by Infrared Emissivity Variability Features. *Remote Sens.* **2023**, *15*, 5132. https://doi.org/10.3390/rs15215132

Academic Editors: Filippo Catani, Jinsong Huang, Faming Huang and Shuihua Jiang

Received: 28 July 2023
Revised: 14 October 2023
Accepted: 17 October 2023
Published: 27 October 2023

Copyright: © 2023 by the authors. Licensee MDPI, Basel, Switzerland. This article is an open access article distributed under the terms and conditions of the Creative Commons Attribution (CC BY) license (https://creativecommons.org/licenses/by/4.0/).

1. Introduction

Loose slopes, such as waste dump slopes and tailings pond slopes, are special slope forms [1,2]. Loose-slope landslides have the characteristics of large volume, fast speed, and long moving distance and are also accompanied by the process of rock fragmentation [3]. The identification and differentiation of fragment bodies of different particle sizes is crucial for the delineation of landslides on loose slopes. Infrared thermal imaging is widely used in the monitoring of landslides [4,5]. The infrared brightness temperature (IBT) is captured by a thermal imaging camera, which is affected both by the physical temperature T_d and surface emissivity ε of the observed target [6].

Scholars have carried out many useful studies on slope landslides. Mori et al. [7] proposed a probabilistic framework to evaluate the landslide runout hazard caused by loosely filled slope failure using the smooth particle hydrodynamics (SPH) method. Cuomo

et al. [8] selected the generalized plasticity model to quantitatively evaluate soil mechanical responses under unsaturated and saturated conditions. Wei et al. [1] innovatively conducted multiple remote sensing techniques to outline the landslide hazard zone of the Xudonggou dump *site*. Bao et al. [9] indicated that as C_v (sediment concentration by volume) decreased, the speed of sliding mass increased, and the run-out distance of a landslide increased. Han et al. [10] demonstrated that the stability of loose accumulation bodies was more clearly influenced by rainfall intensity. Cao et al. [11] discovered that the shear strength of loose dump bodies was significantly dependent on the water content, freeze-thaw cycle, pore pressure, and gradation of the dump soil. Okada et al. [12] suggested that combining surface geophysical surveys with other methods, such as airborne surveys and satellite observations, as an effective method to detect landslide-prone zones in vast areas may effectively locate areas that initially did not appear to be different from the surrounding environment but had a high landslide risk. Chen et al. [13] solved the problem of accurately locating sliding surfaces with tensile cracks in multistage landslide stability analysis and presented a new search method for multistage sliding surfaces: the discontinuous dynamic strength reduction method (DDSRM). Cao et al. [14] proposed a smoothed particle hydrodynamics (SPH) method combined with the Mohr–Coulomb model to study the dynamic characteristics of the landslides that occurred during the destruction of dumps. Huang et al. [15] indicated that the occurrence of landslides can be attributed to increasing incision depth and potential landslide energy. Greco et al. [16] compared two landslides (1999 and 2019) on near slopes through mathematical modeling and found that landslide predisposing conditions were controlled by the soil moisture profile. Huang et al. [17,18] utilized the uncertainty of non-landslide sample selection to represent the uncertainty of landslide susceptibility prediction and indicated that LSP considering different landslide types was superior to that taking only a single type of landslide into account.

Infrared remote sensing has good applications in monitoring slope landslides [19]. According to the research on Remote Sensing Rock Mechanics (RSRM), it is often assumed that the surface emissivity ε is constant at 1.0, which is obviously insufficient [20–22]. Christensen et al. [23,24] found that there was a clear correlation between mineral constituents and their emissivity in the static thermal infrared spectrum observation test of rocks and minerals. It has been known that the particle sizes of solid particles are the main reason for the difference in infrared thermograms of solid materials with different particle sizes, and it is also an important factor for the change in their effective emissivity [25–27]. However, the changing characteristics of the emissivity of rock fragments composed of particles are still unclear. In the previous basic test research on remote sensing rock mechanics [28–32], there was still a lack of in-depth discussion and quantitative analysis of rock particle size on the infrared emissivity of rock fragments, which affected the application practice of remote sensing rock mechanics and the scientific understanding and abnormal interpretation of rock IBT observation results.

Factors controlling the measured infrared emission characteristics of rocks include object properties like physical temperature and surface morphology, as well as observation settings like orientation. The effects of zenith angle and azimuth angle on observation results in satellite infrared observations cannot be ignored [33–35]. In the previous basic tests of rock remote sensing mechanics and infrared practical monitoring, the effect of zenith angle and azimuth angle observation was often ignored. In fact, the observation direction of the infrared thermal imager relative to the rock objects (rock specimens, rock slopes, ore heaps, gangue hills, and tailings dams) is multi-faceted, and the change in direction will inevitably lead to a difference in rock emissivity and affect the IBT observation value to a certain extent.

Therefore, in experimental and practical monitoring, it is necessary to reveal and eliminate IBT differences caused by changes in rock emissivity through the process of angle normalization. Preliminary research has shown the influence of fragment sizes on the measured equivalent emissivity ε_f under strong background radiation [36]. The

equivalent emissivity ε_f changing with fixed background radiation intensity should also be quite focused.

In this research, rock fragment combinations with different grain sizes are prepared, and thermal infrared imaging observation tests with multiple grain sizes, angles, and directions are carried out. By introducing the target pseudo-emissivity, including the influence of strong indoor background radiation, the pseudo-emissivity of fragments with different grain sizes and the pseudo-emissivity deviation caused by directional and angular effects are calculated. Based on this, the calculation model of the pseudo-emissivity of fragments after the zenith angle normalization is deduced, and the pseudo-emissivity of fragments with different particle sizes is obtained. Finally, the variation pattern of pseudo-emission of rock fragments with the particle size of the dispersed material is revealed.

2. Infrared Observation Test

2.1. Test Design

The commonly used infrared observation methods in practice mainly include remote sensing satellites and unmanned aerial vehicles. We have designed two experiments to simulate the observations from the two platforms. One is to simulate remote sensing satellite ground observation (Figure 1a), with a "$*$" shape swing and observation angles θ of four observation lines (Lines 1 to 4, Figure 1a) range changes in the bands of $[-20°, 20°]$, which is referred to as a small angle observation test (E1, Table 1). The other is to simulate unmanned aerial vehicles equipped with infrared thermal imagers for observation with a distribution of measurement points in a "$\times$" shape. The observation angles θ of six points (Points 1 to 6, Figure 1b) range from 20° to 50°, which is a large-angle observation test (E2, Table 2).

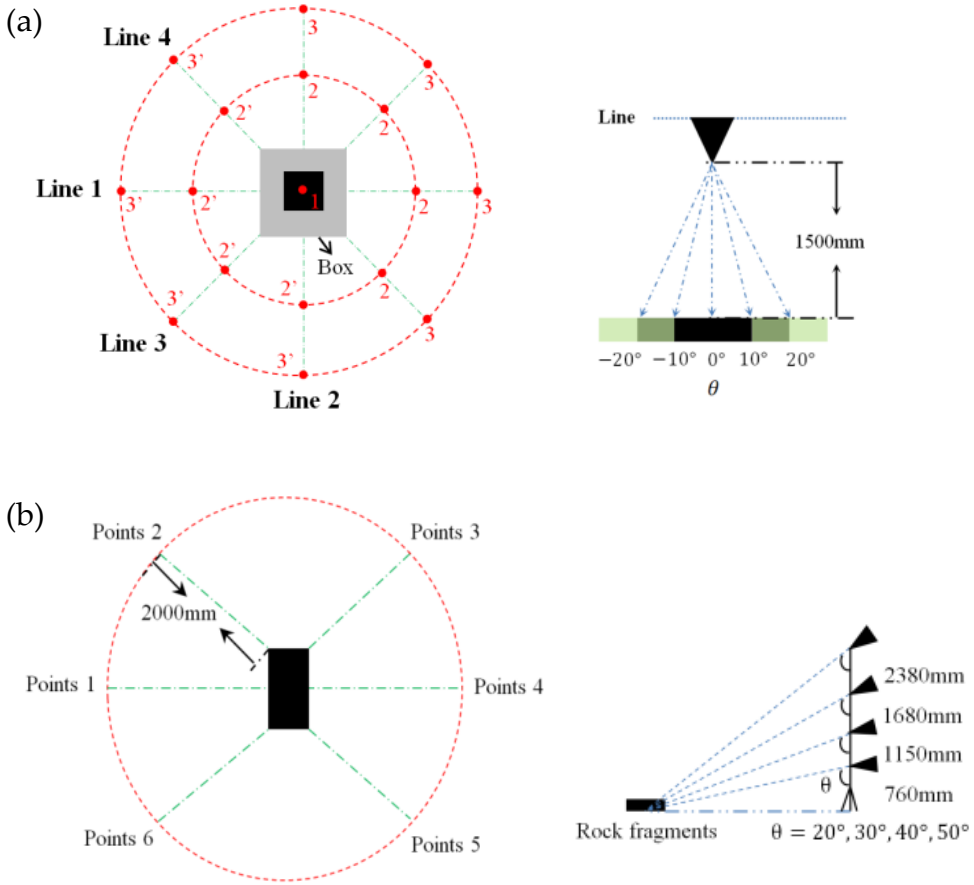


Figure 1. The schematic diagram of the infrared imaging observation test. ((**a**), small angle changes of E1; (**b**), larger angle changes of E2).

Table 1. Observation parameters table for the small angle change test (E1).

Observation Points	Observation Lines	H^*/mm	D^{**}/mm	θ^{***}/°
1	Line 1–4	1500	0	0
2			264.5	10
2′			264.5	−10
3			546.0	20
3′			546.0	−20

H:* Observation lens and debris stage height. *D***: The horizontal distance between the observer lens and the debris stage. *θ****: The situation of the observation zenith angle.

Table 2. Observation parameters table for the larger angle change test (E2).

Observation Points	H^*/mm	D^{**}/mm	θ^{***}/°
Points 1~6	2380	2000	20
	1680		30
	1150		40
	760		50

*H**: Observation lens and debris stage height. *D***: The horizontal distance between the observer lens and the debris stage. *θ****: The situation of the observation zenith angle.

The test *site* is shown in Figure 2. In E1 (Figure 2a), a small angle change observation test, the infrared thermal imager is fixed above the stage using a herringbone ladder, and the stage is placed in a black box in order to isolate the influence of surrounding background radiation. The black box is placed on the flat car, and the flat car moves along the calibrated position to form an observation zenith angle change of $[-20°, 20°]$. E2 (Figure 2b), a large angle change observation test in which the infrared thermal imager adjusts the observation height using a lifting frame to form an observation zenith angle change of $[20°, 50°]$.

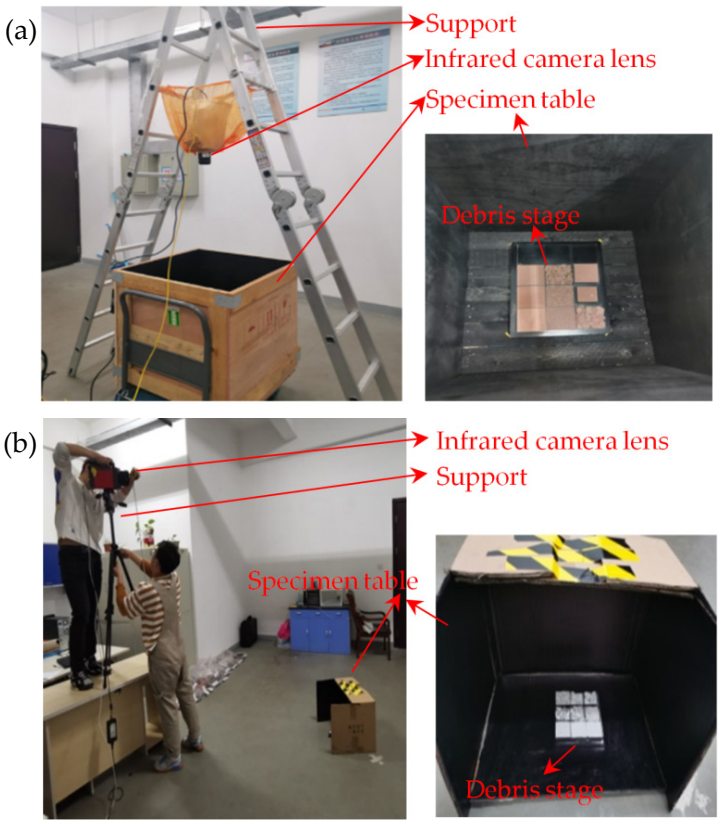


Figure 2. Testing *site* photograph. (**a**), E1; (**b**), E2).

In fact, specimens of rock fragments with different particle sizes are arranged on the stage according to a matrix. In the same observation field of view, the thermal imager has a view deviation from the actual zenith angle θ' of the different particle sizes of the rock fragments. The calculation example is shown in Figure 3, where the position of the rock fragment sample on the loading platform is fixed and the deviation value of the same observation zenith angle θ is also determined (Table 3).

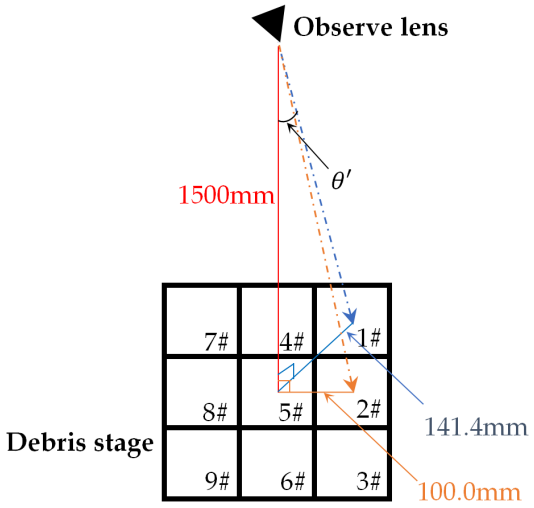


Figure 3. Geometric diagram of θ'-bza deviation.

Table 3. Statistical tables of the difference between θ'-bza and θ-bza.

		Actual Zenith Angle θ' (°)									Test
		1#	2#	3#	4#	5#	6#	7#	8#	9#	
Observation zenith angle θ (°)	−20	−14.61	−16.16	−14.61	−16.16	−20.00	−23.84	−25.39	−23.84	−25.39	E1
	−10	−4.61	−6.16	−4.61	−6.16	−10.00	−13.84	−15.39	−13.84	−15.39	
	0	5.39	3.84	5.39	3.84	0.00	−3.84	−5.39	−3.84	−5.39	
	10	15.39	13.84	15.39	13.84	10.00	6.16	4.61	6.16	4.61	
	20	25.39	23.84	25.39	23.84	20.00	16.16	14.61	16.16	14.61	
	20	21.80	21.80	21.80	20.00	20.00	20.00	19.90	19.90	19.90	E2
	30	31.18	31.18	31.18	30.00	30.00	30.00	28.71	28.71	28.71	
	40	41.30	41.30	41.30	40.00	40.00	40.00	38.66	38.66	38.66	
	50	51.40	51.40	51.40	50.00	50.00	50.00	48.58	48.58	48.58	

2.2. Preparation of Rock Specimens

(1) Preparation of rock fragments specimens

A jaw crusher is used to break rock mechanically, and iron screen meshes with different apertures are used to screen the broken rock fragments. Granite, marble, and sandstone are, respectively, used to prepare rock fragments of seven sizes.

In order to compare easily, target rock specimens with polished surfaces and I-type fracture surfaces were prepared separately, and together with the corresponding seven types of rock fragments, a nine-grid matrix was formed and placed on the observation platform for overall infrared imaging observation. Table 4 shows the particle sizes and number of rock fragments from different target rock specimens, and Figure 4 shows the actual arrangement of rock specimens in multi-granularity combined observation.

Table 4. Information on rock fragment particle sizes and their numbers.

Num.	Name	Information	Num.	Name	Information	Num.	Name	Information
1#	Intact rock	Surface buffing	2#	Fracturing face	I type of crack surface	3#	Large block	25 mm
4#	Medium block	13 mm	5#	Small block	5 mm	6#	Large sand	1 mm
7#	Medium sand	0.5 mm	8#	Small sand	0.2 mm	9#	Tiny sand	0.1 mm

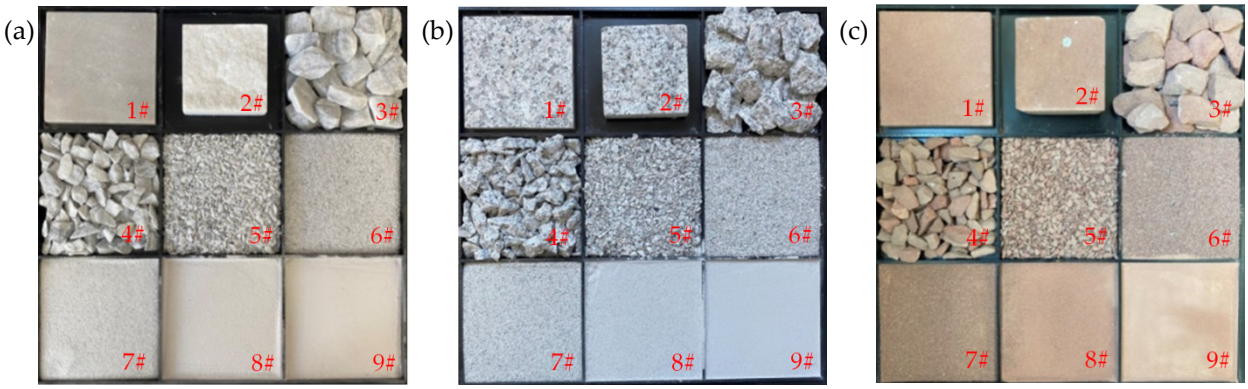


Figure 4. Reality images of multi-size combined observations. ((**a**), marble; (**b**), granite; (**c**), sandstone).

(2) Lithological identification

Rock orthogonal polarization microscopy tests are carried out to measure the mineral composition and content. Figure 5 shows the distribution and location of the main minerals in three types of rocks, with the specific results as follows:

- *Marble* belongs to metamorphic rock, which is obviously layered with *a* fine grain structure and particle size distribution *ranging* from 0.1 mm to 1.5 mm. The main mineral components are calcite, dolomite, and quartz. Calcite, with *its* massive structure, accounts for from 45% to 50%. Dolomite, with a block-like structure, accounts for from 35% to 40%. Quartz, with *its* granular structure, accounts for from 10% to 20%.
- *Granite* belongs to *the* igneous rock *family, has* a fine *microstructure,* and is brownish white. The main mineral components are plagioclase, potassium feldspar, quartz, hornblende, and biotite. Plagioclase, block-like with twin structure, from 0.5 mm to 3 mm, accounts for from 35% to 40%. Potassium feldspar, *with a* block-like structure *ranging* from 0.5 mm to 5 mm, accounts for 25% to 30%. Quartz, with a granular structure and an average particle size of 1.5 mm, accounts for from 20% to 25%. Hornblend, with a columnar structure and green mud metamorphism, accounts for from 3% to 5%. Biotite, with *its* schistose structure, accounts for from 2% to 3%.
- *Sandstone* belongs to sedimentary rock, with medium- and fine-grained minerals in massive *structures*. Among them, *fragment* particles with a particle size of from 0.05 mm to 0.1 mm account for about 40%, and *fragment* particles with a particle size of from 0.1 mm to 0.5 mm account for about 60%. The main minerals are clasolite, such as quartz and feldspar, and a small amount of muscovite.

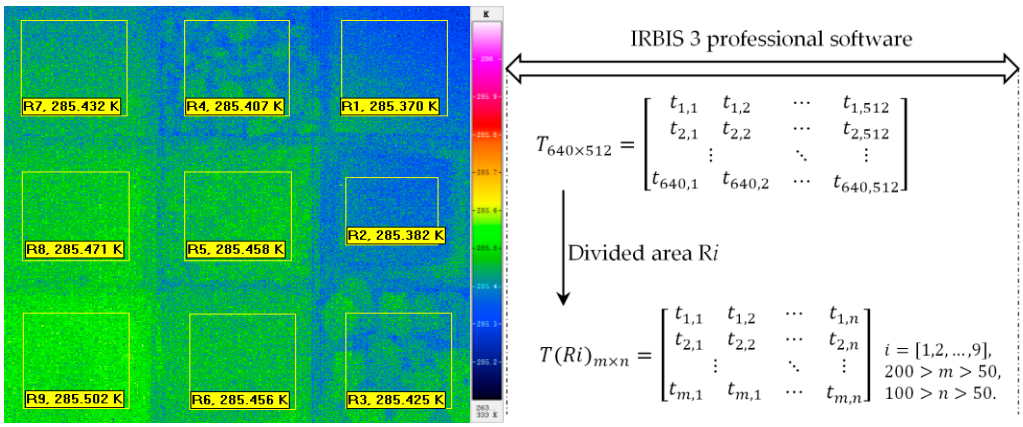


Figure 5. Diagram of IBT extraction for each target. (R1–R9 are the circle areas of 1#–9#).

2.3. Observation System

When the test started, the indoor temperature was controlled at 285.25 ± 0.1 K, and the accuracy was 0.1 K. The test was carried out after 10PM, and the lights were turned off, personnel were prohibited from moving around, shading curtains were closed, and a constant room temperature was strictly controlled during the observation period. The parameters of the thermal imager and lens are as follows:

- *Infrared thermal imager*: *The* Infra Tec 8325 type medium-wave infrared thermal imager is produced by the German Infotec formula, with observation bands ranging from 3.7 to 4.8 μM. The highest resolution of thermal images is 640 pixels × 512 pixels, *the* sampling rate is up to 120 P/s, *and* the temperature recognition accuracy is 0.1 K.
- *Standard lens*: Model is M83287; focal length is 25 mm; focal length ratio is 2.0; field of view angle is $(21 \times 17)^\circ$. When the observation distance is 1 m, the maximum plane size of the observation object reaches 384 mm × 307 mm, *the* instantaneous field of view is 0.6 mrad, *and the* focusing range is 0.3 m to infinity.

3. Test Results and Analysis

3.1. Extraction of Rock Fragments Target IBT

Delineate the analysis area (polished rock surface 1#, I-type fracture surface 2 #, rock fragments 3#–9#) from the thermal image, and extract the IBT (simplified as T) values of different observation targets (Figure 5). Read the AIBT (average infrared brightness temperature) T of rock fragments from 1# to 9# separately $T_i(j,\ k)$ (i is the rock fragments number; $i = 1, 2, ..., 9$; j represents the observation line, $j = 1, 2, 3, 4$; k represents the observation angle, $k = 0^\circ$, 10°, -10°, 20°, -20°, 30°, 40°, 50°). Area R2 is much smaller than other R*i* (R2 in Figure 5). The reason is that R2 is the I type of crack surface, and the size of rock fragment R2 is significantly less than others R*i* (Table 4, Figure 4).

3.2. Directional Effect of Rock Fragments IBT

According to Planck's law (Blackbody radiation law), the emission of 300 K features in the observation band is 3.7–4.8 μm, and the emission is about 1/8 of 8–12.5 μm, and the environmental radiation cannot be ignored. Therefore, the observed value of rock chip IBT T_i is actually the sum of the true value of IBT T_{Vi} and the environmental radiation ξ_i, that is,

$$T_i = T_{Vi} + \xi_i \tag{1}$$

The infrared observation testing model was effectively shading, and the ambient radiation value ξ_i was the same under the same window (the same observation zenith angle θ and the orientation of the measurement line). In the same window, the actual zenith angle θ' and actual direction faced by different fragment targets are different (Table 3, Figure 3). The rock targets on the stage are arranged in a nine-square grid with fixed relative positions between the fragment targets. ΔT represents the difference between the observed values of a certain orientation $T_i(j,k)$ and the mean of the observations in all orientations $\overline{T_i}$, that is,

$$\Delta T = T_i(j,\ k) - \overline{T_i} = (T_{Vi} + \xi_i) - \left(\overline{T_{Vi}} + \xi_i\right) = T_{Vi} - \overline{T_{Vi}} \tag{2}$$

It is known from the above equation that after effective shading treatment, the environmental radiation of the same inspection is enhanced to a fixed value, and the ΔT obtained by the above formula can reflect the change in the true value of the target rock chip IBT. In IBT observation tests, if the directionality of indoor strong background radiation causes the IBT in this direction to differ greatly from other orientations, it is called the dominant direction of background radiation.

Figures 6–8 are the IBT variation curves of marble, granite, and sandstone with observation angle and the difference between the same observation zenith angle θ and different measurement lines (azimuth). In Figures 6–8, ΔT is represented as bar graphs, and T is referred to $\overline{T_{Vi}}$, and represented as diamond.

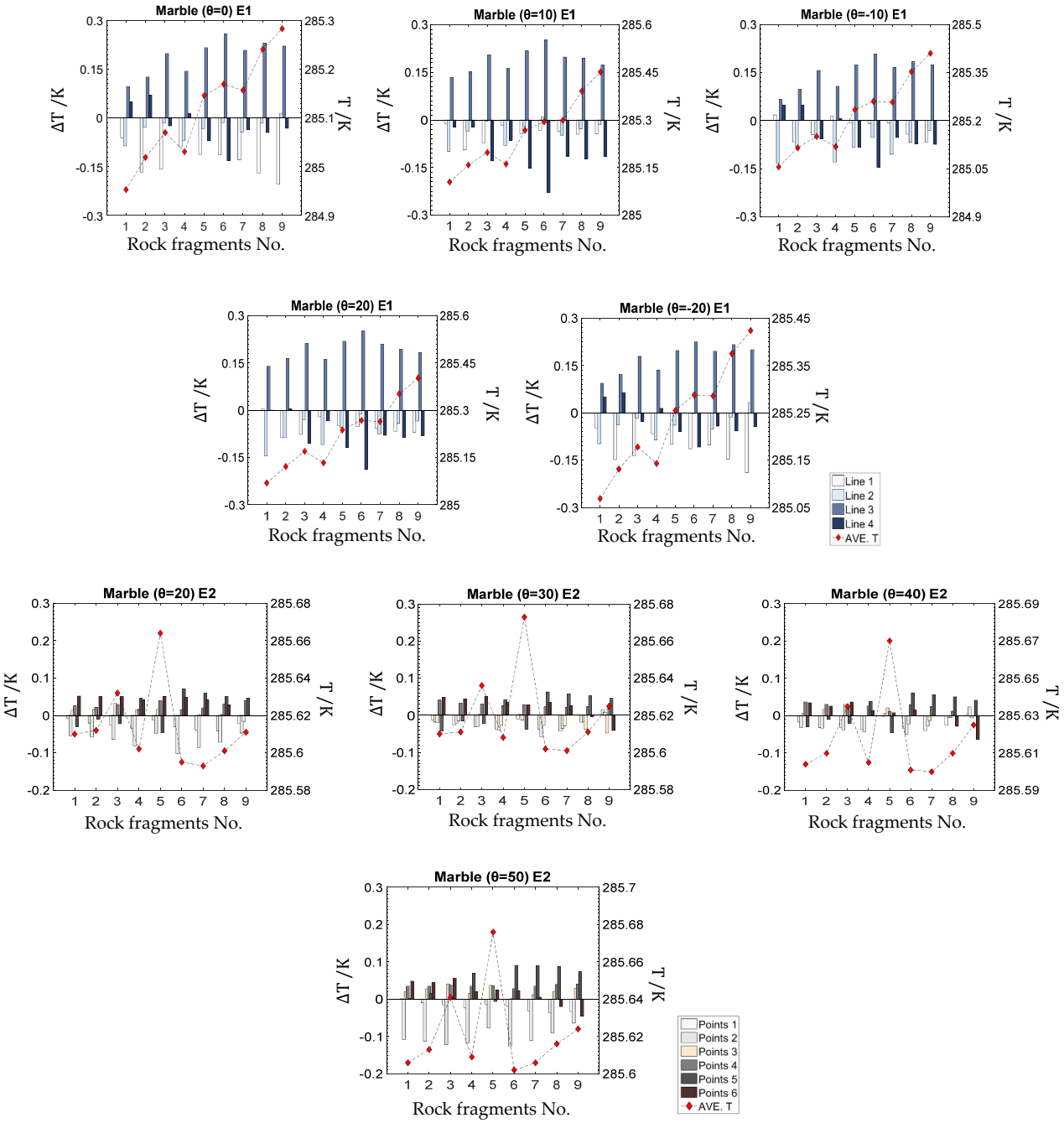


Figure 6. IBT changes the characteristics of marble specimens on four lines according to different θ-bza.

- *Marble* (Figure 6): E1 ($\theta \in [-20°, 20°]$), Line 3 is the most different from other measurement lines. All target specimens of Line 1 in $\theta = 0°$, 6# target specimens of Line 4 in $\theta = 10°$ ($\theta' = 6.16°$), 6# target specimens of Line 4 in $\theta = -10°$ ($\theta' = -13.84°$), and 9# target specimens of Line 1 in $\theta = 20°$ ($\theta' = -25.39°$), etc. showed differences. In E2 ($\theta \in [20°, 50°]$), Point 2 is the most distinct from other measurement points. The 9# target sample in $\theta = 40°$ ($\theta' = 34.61°$) and the target sample 1# in $\theta = 50°$ ($\theta' = 55.39°$) also showed heterogeneity.
- *Granite* (Figure 7): E1 ($\theta \in [-20°, 20°]$), Line 3 differs most significantly from other measurement lines. 1# target specimens ($\theta' = 5.39°$) and 2# target specimens ($\theta' = 3.84°$) of Line 4 in $\theta = 0°$, 1# target specimens ($\theta' = -4.61°$) and 2# target specimens ($\theta' = -6.16°$) of Line 4 in $\theta = -10°$. In E2 ($\theta \in [20°, 50°]$), the overall heterogeneity of

Points 6 is the most obvious. The differences between the 3# target sample of Points 1 in $\theta = 20^\circ$ ($\theta' = 25.39^\circ$) and the target sample of Points 3 in 30° ($\theta' = 35.39^\circ$) in $\theta = 30^\circ$ are also obvious.

➢ *Sandstone* (Figure 8): In E1 and E2, the integrity and consistency of ΔT of each particle size target sample at $\theta \in [-20^\circ, 50^\circ]$ are good. The differences between the 1# target sample of Line 1 in $\theta \in [-20, 20]$ ($\theta' \in [-14.61, 25.39]$), the 1# target sample of Points 5 in $\theta \in [20, 50]$ ($\theta' \in [25.39, 55.39]$), and the 6# target sample of Points 5 in $\theta = 30^\circ$ ($\theta' = 26.16^\circ$) are also obvious.

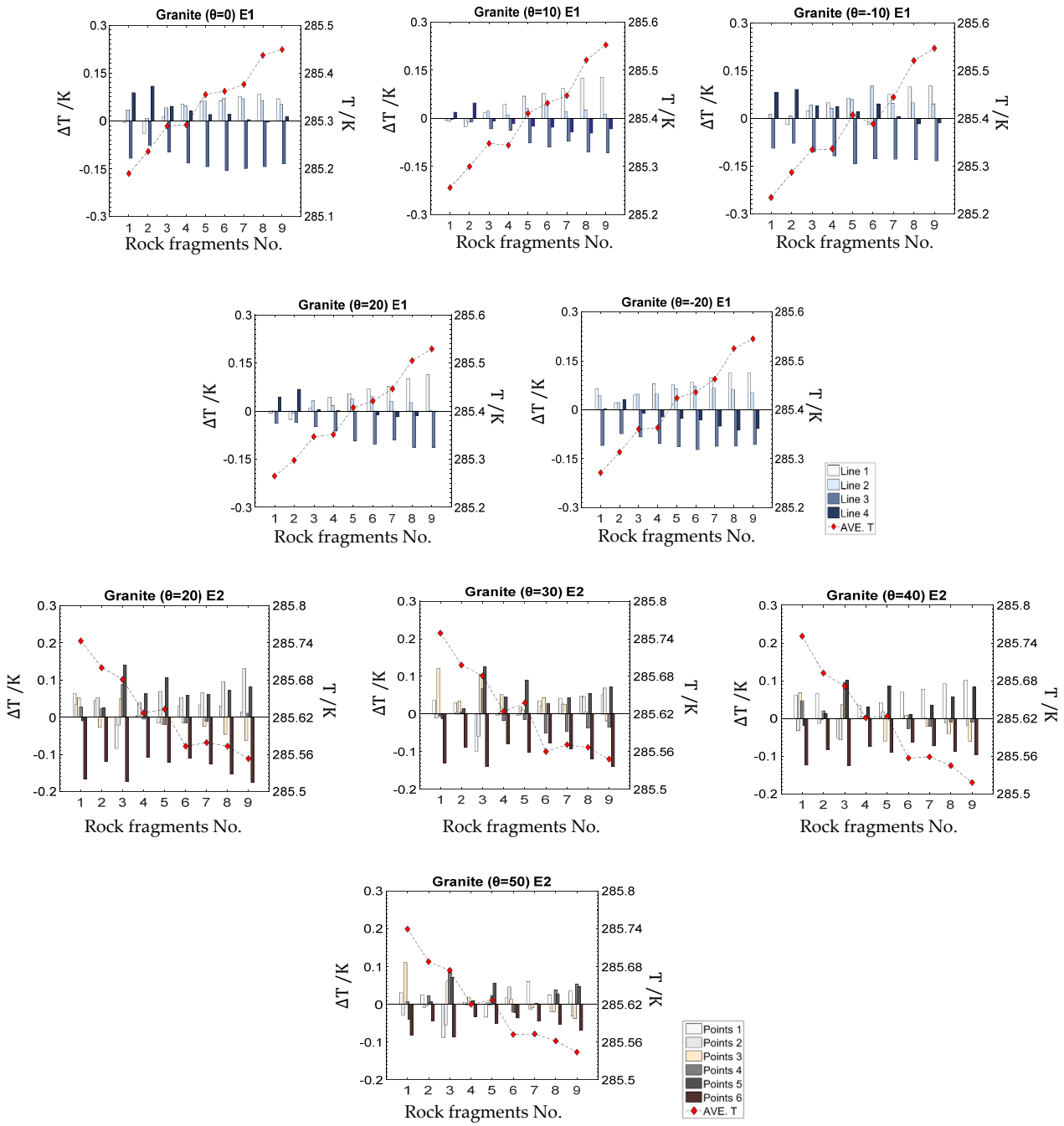


Figure 7. IBT changes the characteristics of granite specimens on four lines according to different θ-bza.

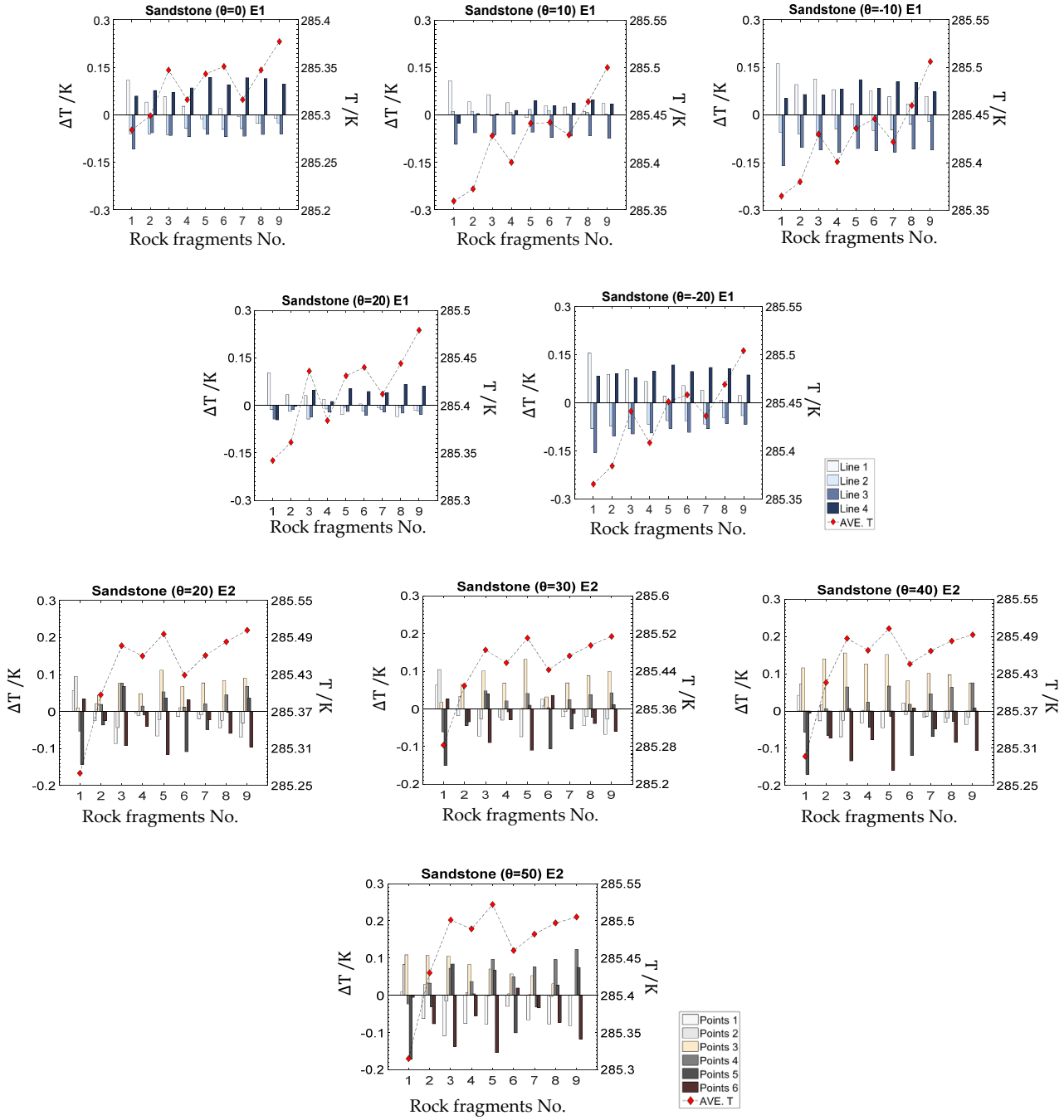


Figure 8. IBT changes the characteristics of the sandstone specimen on four lines according to different θ-bza.

Therefore, the dominant direction of background radiation in this test is located directly below the stage.

3.3. Angle Effect of IBT

In the test, shading and isolating the surrounding background radiation were effectively treated, and the difference value of IBT in different directions was controlled within the range of ±0.2 K. The average values of IBT observations at the same zenith angle θ and different azimuths were used to analyze and explore the angular effect of IBT. The angle effect is for observing the zenith angle θ. θ changed curve was observed in E1 ($\theta \in [-20°, 20°]$, left side in Figure 9) and E2 ($\theta \in [20°, 50°]$, right side in Figure 9).

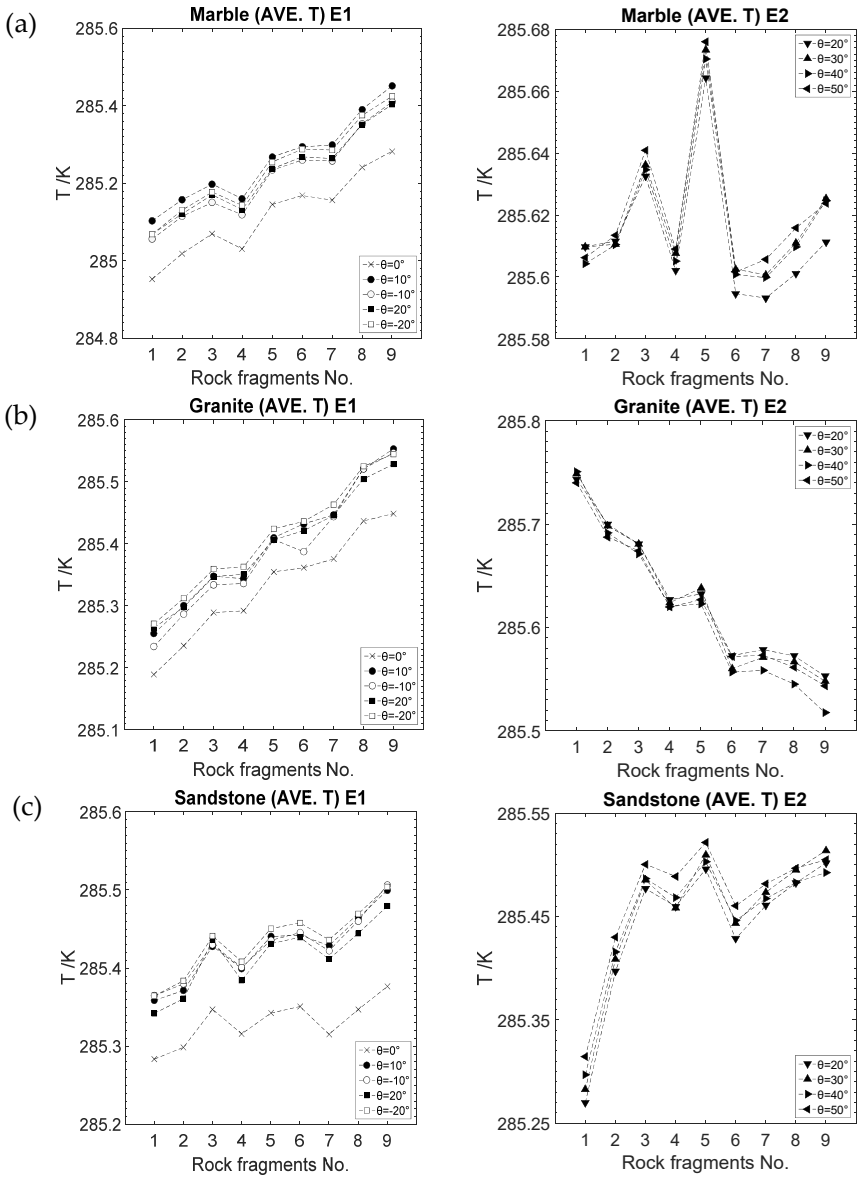


Figure 9. IBT changes the characteristics of different rock specimens and different θ-bza. ((**a**) Marble (AVE. T); (**b**) Granite (AVE. T); (**c**) Sandstone (AVE. T)).

- *Marble (*Figure 9*a)*: E1, the maximum value of $T_i(j,k)$ is 9#, the minimum value is 1#, 4#. The trend of T change is "rising (1#→3#) → slowly falling (3#→4#) → ladder ascending (4#→9#)". E2, $T_i(j,k)$ maxima is 3#, 5#, 9#, minimum values 1#, 4#, 6#, T change is the trend of "rising (1#→3#)→step up (3#→6#)→slightly climb (6#→9#)".
- *Granite (*Figure 9*b)*: E1, the maximum value of $T_i(j,k)$ is 9#, the minimum value is 1#. The trend of T change is an overall rise. E2, the maximum value of $T_i(j,k)$ is 1#, the minimum value is 9#. The trend of T change shows an overall step down.
- *Sandstone (*Figure 9*c)*: E1, the maximum value of $T_i(j,k)$ is 3# and 9#, the minimum value is 1#. The trend of T change shows a small increase in volatility. E2, the maximum value of $T_i(j,k)$ is 3#, 5# and 9#, the minimum value is 1# and 6#. T change is the trend of "rapid rise (1#→3#) → small fluctuation (3#→9#)". Furthermore, there is also a linear correlation with T and fragment size in small angle changes of E1 (Left side in Figure 9), but the correlation in larger angle changes of E2 (Right side in Figure 9) is not obvious. The main reason is that the angle effect is different in different minerals. While the observed zenith angle θ is in small change, the angle effect of the mineral has little influence and is greatly influenced by larger angles.

4. Analysis of Rock Pseudo Emissivity Changes

4.1. Definition and Its Solution Process of Pseudo-Emissivity

The radiation ejection degree M of blackbody obtained from the surface physical temperature T_d of the feature and its surface emissivity ε_λ integral, as follows,

$$M_B(T) = \int_0^\infty M(\lambda, T)d\lambda = \sigma T^4 \tag{3}$$

where σ is the Stephen-Boltzmann constant, $5.67 \times 10^{-8}\mathrm{W/m^2 \cdot K^{-4}}$. λ is the wavelength of the radiation wave. T is the radiation temperature.

Generally, radiation detectors are often observed in the fixed band, such as $[\lambda_i,\ \lambda_j]$. The upper Equation will make the following transformations:

$$M(\lambda_i,\ \lambda_j) = \frac{E(\lambda_i,\ \lambda_j)}{E(0,\ \infty)} \int_0^\infty M(\lambda, T_d)d\lambda = \sigma \cdot \varepsilon(\lambda_i,\ \lambda_j) {T_d}^4 \tag{4}$$

where $M(\lambda_i,\ \lambda_j)$ is the radiation flux in the observation band of $[\lambda_i,\ \lambda_j]$. $E(\lambda_1,\ \lambda_2)$ is the radiation energy in $[\lambda_i,\ \lambda_j]$. $E(0,\ \infty)$ is the radiation energy of the full-wave band. $\varepsilon(\lambda_i,\ \lambda_j)$ is the infrared emissivity in $[\lambda_i,\ \lambda_j]$. $E(\lambda_1, \lambda_2,\ T_d)$ is the radiation energy in $[\lambda_i,\ \lambda_j]$ as the physical temperature, T_d. $\varepsilon(\lambda_1,\ \lambda_2)$ is the surface emissivity in $[\lambda_i,\ \lambda_j]$. T_d is the physical temperature of the rock surface.

When a ground object is observed by a thermal imager, infrared bright temperature (IBT) is the abbreviation of the bright radiant temperature of the object in the infrared band, which is the temperature corresponding to the isoenergetic radiation intensity or radiant flux of the blackbody in the same band. If the infrared thermal imager detects the fixed band $[\lambda_1,\ \lambda_2]$. Infrared bright temperature (IBT) T is solved as follows:

$$T^4 = \varepsilon(\lambda_1,\ \lambda_2) \cdot {T_d}^4 \tag{5}$$

where T is the IBT in the observation band of $[\lambda_1,\ \lambda_2]$. $\varepsilon(\lambda_1,\ \lambda_2)$ the surface emissivity in the observation band of $[\lambda_1,\ \lambda_2]$.

In this test, the radiation flux received by the infrared thermal imager comes not only from the emission of the rock chips but also from the surrounding environment when it is irradiated into fragments. Therefore, it can be seen from Equation (5) that the IBT (T) measured by the thermal imager consists of the following two parts:

$$T^4 = \varepsilon(\lambda_1,\ \lambda_2) \cdot {T_d}^4 + \varepsilon_{sur} \cdot [1 - \varepsilon(\lambda_1,\ \lambda_2)] \cdot {T_{sur}}^4 \tag{6}$$

where T is the measurement of rock fragments in IBt. $\varepsilon(\lambda_1,\ \lambda_2)$ is the surface emissivity of the target fragments. T_d is the surface physical temperature of the target cutting. ε_{sur} is the emissivity of the surrounding environment of the observed object. T_{sur} is the physical temperature of the surrounding environment of the observed object.

Since the rock fragment specimens have been left in the laboratory for a long time before the test, the temperature equilibrium between the rock fragment specimens and their surrounding environment has been reached, so it can be assumed that $T_d = T_{sur}$.

Thus, Equation (6) can be simplified to:

$$T = \sqrt[4]{(\varepsilon(\lambda_1,\ \lambda_2) + \varepsilon_{sur} - \varepsilon(\lambda_1,\ \lambda_2) \cdot \varepsilon_{sur})} \cdot T_d \tag{7}$$

By transforming Equation (7), it can be obtained that,

$$\varepsilon(\lambda_1,\ \lambda_2) + \varepsilon_{sur} - \varepsilon(\lambda_1,\ \lambda_2) \cdot \varepsilon_{sur} = \frac{T^4}{{T_d}^4} \tag{8}$$

It can be seen from Equation (8) that the emissivity calculated by using the observation value T of rock chip IBT and its physical temperature T_d is influenced comprehensively by

the true emissivity of target rock fragments ε and the ε_{sur} of environmental radiation emissivity. The emissivity ε_i is called rock chip pseudo-emissivity, and the pseudo-emissivity is related to the test observation environment, namely,

$$\varepsilon_i = \varepsilon(\lambda_1, \lambda_2) + \varepsilon_{sur} - \varepsilon(\lambda_1, \lambda_2) \cdot \varepsilon_{sur} \quad (9)$$

In the infrared observation test of rock fragments in this study, the observed environmental factors include the inner surface of the wooden box, the ceiling of the laboratory, the thermal imager, and the observers. In the process of the infrared observation test, the doors, windows, and curtains are closed, the lights are extinguished, and the personnel are stationary. The environmental factors are basically unchanged, so its emissivity ε_{sur} can be regarded as unchanged.

4.2. Variation Characteristics of Rock Chip Pseudo Emissivity

The rock chip objects of different grain sizes on the stage are arranged in a nine-square grid, and the relative positions of different rock chip objects and the observation environment are different, but the relative positions are fixed. For the same fragment object (i), the IBT observed in different directions and under different zenith angle conditions (j) is influenced comprehensively by the directional emissivity (including the combined influence of azimuth and zenith angle) and the observation environment of the fragment object, so it is different. If the influence of the local shift of the camera pose is ignored, the observation environment of the rock chip object can be regarded as completely identical. At this point, the difference in IBT is only caused by the difference in the directional emissivity of the fragments.

To eliminate the influence of directional emissivity differences, the average value of infrared pseudo emissivity $\varepsilon_i(i, j)$ of rock chip objects under different azimuth and zenith angle conditions was taken as the infrared pseudo-emissivity ε_i of rock chip objects in the observation environment. Accordingly, the difference in infrared pseudo-emissivity of rock chip objects $\Delta\varepsilon$ in different orientations and different zenith angles in the observation environment can also be obtained, namely,

$$\Delta\varepsilon = \varepsilon_i(i, j) - \varepsilon_i \quad (10)$$

Using the IBT observations of rock targets under the same working conditions, the difference analysis of the same observation zenith angle and different survey line directions (azimuth) is the basis for solving the IBT difference question. It is supposed that the petrophysical temperature is equal to the room temperature ($T_d = 285.25$ K). According to the observation results of the IBT test, the deviation value of the pseudo-emissivity of rock fragments $\Delta\varepsilon$ caused by the observation conditions is solved by Equation (6), and the extreme value caused by the direction effect and angle effect is calculated (Table 5). It can be seen that the observation conditions of θ of the zenith angle of multiple observations will have a maximum deviation of IBT $\Delta T = 0.260$ K, corresponding to a pseudo-emissivity ε maximum deviation $\Delta\varepsilon = 6.5 \times 10^{-3}$.

Table 5. Distribution statistics of rock fragments.

Rock Specimen	The Extreme Value of ΔT (K)		The Extreme Value $\Delta\varepsilon$ (10^{-3})	
	Maximum	Minimum	Maximum	Minimum
Marble	0.26	−0.17	3.7	−6.5
Granite	0.13	−0.18	4.1	−5.5
Sandstone	0.16	−0.17	2.6	−2.4

4.3. Pseudo-Emissivity Variation Features Based on Zenith Angle Normalization

(1) Pseudo-emissivity solving algorithm based on zenith angle normalization

The change in emissivity (specific radiance) is greatly affected by the zenith angle, so it is important to use the zenith angle to revise the target emissivity. Multi-zenith-angle observation tests were carried out to obtain more effective radiation information about the target object, which provided feasibility for determining the observation value of the target pseudo-emissivity [36,37]. To explore the influence of target emissivity by the change of θ of observed zenith angle, it is necessary to normalize zenith angle and unify between $\left[-20^{\circ}, 20^{\circ}\right]$ and $\left[20^{\circ}, 50^{\circ}\right]$, to eliminate the influence of direction effect and angle effect. Zenith angle θ corresponds to an infrared radiation temperature $T(\theta)$, and each $T(\theta)$ corresponds to a target pseudo-emissivity value $\varepsilon(\theta)$.

Referring to the relationship between the physical temperature and the emissivity of the target object under the condition of multi-observation zenith angle [38], the observed $\varepsilon(\theta)$ value of the change in zenith angle can be solved as follows:

$$\varepsilon(\theta) = \sum_{i}^{\theta} f(\theta) \cdot \varepsilon(\theta_i) \tag{11}$$

where i represents the change value of the observation zenith angle θ. $f(\theta)$ is the directionality index of the pseudo emissivity of rock fragments considering the change of θ. $\varepsilon(\theta_i)$ is the measured value of the emissivity of the target object θ_i without considering the change of θ.

As shown in Figure 3 and Table 3, under the influence of the observation orientation in the infrared imaging observation test, the actual zenith angle θ' is not the same for the same grain size chip specimen from different observation zenith angles θ. The calculation of $f(\theta)$ is simplified in this paper. The mean θ' and θ are used to participate in the calculation, but the change in the actual value of θ' is ignored.

This paper can only simplify the calculation of $f(\theta)$, without considering the change in the actual value of θ', and use the mean θ' and θ to participate in the calculation.

In general, $f(\theta)$ is characterized using the normalized directionality index as follows:

$$f(\theta) = \left(\frac{\varepsilon(\theta) - \varepsilon_{min}}{\varepsilon_{max} - \varepsilon_{min}}\right)^2 \tag{12}$$

where ε_{min} is the minimum emissivity of the target feature without considering the azimuth. ε_{max} is the maximum emissivity of the target feature without considering the azimuth.

(2) Analysis of pseudo-emissivity variation characteristics of rock fragments of different grain sizes based on zenith angle normalization.

The pseudo-emissivity value based on zenith angle normalization $\varepsilon(\theta)$ is obtained by solving Equation (11), which effectively unified the two infrared imaging observation tests (small angle changes of E1, Figure 1a; larger angle changes of E2, Figure 1b). Approximately 2# is the tensile natural fracture surface formed by the I-type fracture test, and the undulation degree of the fracture surface is relatively gentle and uniform (2#, Figure 3). Supposed that only diffuse reflection occurs on the surface of 2# in the fragments, which is a Lambertian body (ideal diffuse reflector). $\varepsilon_i(j,k)$ of other target fragments are minus $\varepsilon_2(j,k)$ of 2#, and their changes relative to the ideal diffuse reflector are discussed. ξ_i represents the degree to which this particle size $\Delta\varepsilon_i$ deviates from the standard deviation $\Delta\varepsilon$ of all fragments pseudo emissivity arrays in this lithological target sample.

$$\Delta\varepsilon_i(j,k) = \varepsilon_i(j,k) - \varepsilon_2(j,k) \tag{13}$$

where $\Delta\varepsilon_i(j,k)$ is the difference between the other $\varepsilon_i(j,k)$ relative to the 2# target sample $\varepsilon_2(j,k)$, $(i = 1,3,4,5,6,7,8,9)$.

$$\xi_i = \Delta\varepsilon_i(j,\ k) - \sigma(\Delta\varepsilon) \tag{14}$$

where ξ_i is the difference between $\Delta\varepsilon_i$ and its standard deviation.$\sigma(\Delta\varepsilon)$) represents the standard deviation of $\Delta\varepsilon_i$.

After observing the normalization of zenith angles, $\varepsilon_i(j,k)$, ξ_i and $\Delta\varepsilon_i(j,k)$ were plotted as curves with the particle size of the bulk (Figure 10), and the change law was summarized as follows:

- *Comparison of complete rock blocks (1# and 2#)*: Approximately 1# appears rock glossy, and 2# appears Type I fracture surface. The roughness of 2# is greater than 1#, and the true emissivity of 2# is greater than 1#. In this test, for $\Delta\varepsilon_1(j,k)$ calculated by using the observations, sandstone is negative and marble rock and granite are positive. The absolute value of ξ_1 in marble and granite is less than ξ_2, while sandstone is just the opposite. The radiation enhancement effect of directional reflection of sandstone background radiation affects the relative relationship between 1# and 2# emissivity observations, while marble and granite do not.
- *Particle size > 1 mm (3#, 4#, 5#)*: The maximum value is $\varepsilon_5(j,k)$ (5#), corresponding to a particle size of 5 mm. ξ_5 for both marble and granite is the maximum, and the maximum value for sandstone is ξ_3. It indicates that when the grain size is >1 mm, the mineral specular reflection of marble and granite specimens affects the actual pseudo-emissivity value, while the influence of specular reflection *on* sandstone is relatively weak.
- *Particle size $\leq$ 1 mm (6#, 7#, 8#, 9#)*: When the particle size of the rock chip decreases to 1 mm or below, its pseudo-emissivity $\varepsilon_i(j,k)$ shows a slight increase trend with the decrease of particle size, and its ξ_i is positively correlated with its particle size. This shows that the mineral specular reflection of the rock chip target is weak when the fragment size is less than 1 mm, and the change law of the pseudo-emissivity of the target can be characterized by roughness.

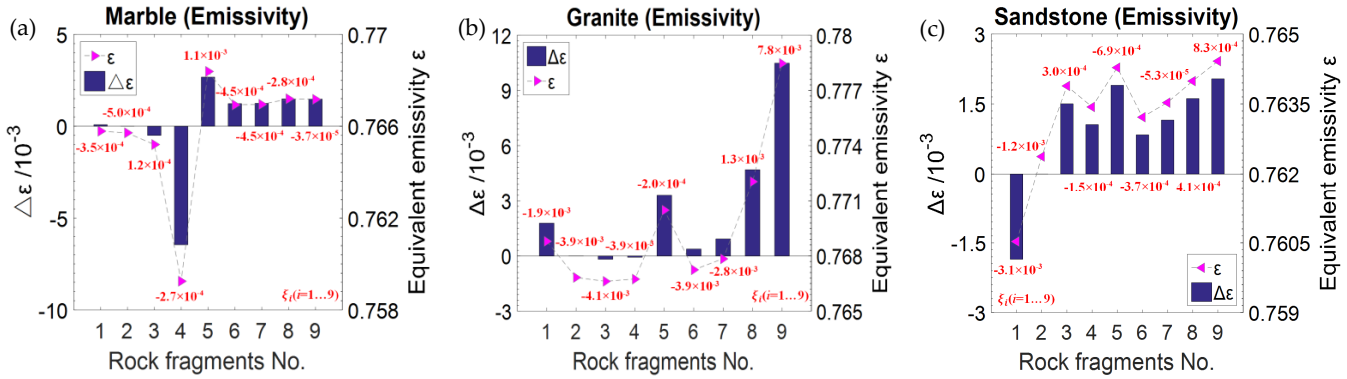


Figure 10. Variation curves of $\varepsilon_i(j,\ k)$, ξ_i and $\Delta\varepsilon_i$ changing with particle sizes after normalized-θbza. ((**a**) Marble (Emissivity); (**b**) Granite (Emissivity); (**c**) Sandstone (Emissivity)).

In summary, after zenith angle normalization, the pseudo-emissivity observations of three rock targets $\varepsilon_i(j,k)$ obtained a relatively uniform change law. When the fragment size is bigger than 1 mm, $\varepsilon_5(j,k)$ of the small block 5# (5 mm particle size) is the largest. When the fragment size is less than 1 mm, $\varepsilon_i(j,k)$ and particle size showed an inverse trend.

4.4. Potential Applications of Fragmentation Identification on Loose Slope Landslides

The landslide susceptibility is a time-variant variable and can be updated using the fresh landslide inventory [39]. Combining the two monitoring methods of remote sensing satellites and unmanned aerial vehicles is more advantageous for landslide monitoring and early warning. To some extent, the effects of direction and angle should be emphasized. This study identified some different features of rock fragments in IBT in the monitoring methods of remote sensing satellites and unmanned aerial vehicles. The IBT of rock mass is determined by the physical temperature, T_d and surface emissivity ε.

In loose-slope monitoring, landslides often manifest as bulky rock flows. Large rock collapses are usually extremely dangerous and often cause catastrophic damage due to rapid movement and long travel distances (Figure 11) [40]. Bulky rocks are distributed on the slopes (Figure 11a) and consist of gravel of different grain sizes (b and c in Figure 11b). These bulky rocks will accelerate sliding during landslides and form large landslide surfaces (Figure 11c). Remote identification of bulky rocks is particularly important.

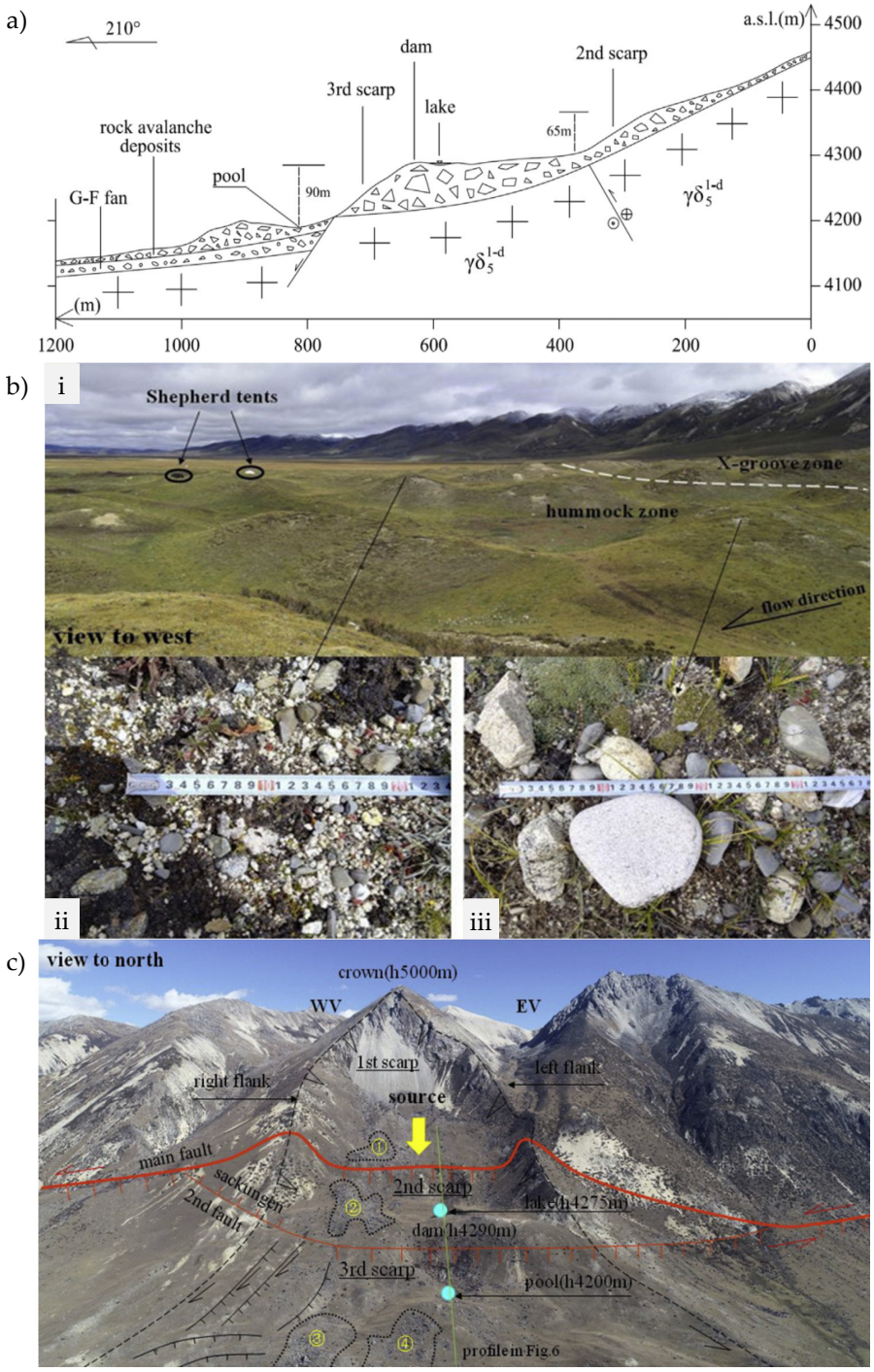


Figure 11. (**a**) Bulky rock distribution on slopes; (**b**) Fluvial gravels mixed with the rock-avalanche blocks in the hummock zone (**i**: hummocky landform of western part of LSB rock avalanche; **ii** and **iii**: small and medium fluvial gravels on hummock top, respectively); (**c**) landslide body distributions (①–④ areas are the block belts detached from each other due to the secondary slide. (WV and EV: the western and eastern glacial valleys) [40].

We concluded that the particle size of bulky rock on the loose slope is closely related to the sliding distance of the landslide. Combined with potential energy, slope angle, and water content to infer the landslide distance, the landslide impact area is delimited in advance to provide life and property evacuation areas for irreversible landslide disasters.

5. Conclusions

In this paper, the indoor strong background radiation is approximated as an invariant constant by effective shading treatment, and the pseudo-emissivity is introduced. The indoor infrared brightness temperature (IBT) observation test of marble, granite, and sandstone fragments with different grain sizes was carried out, and the change rule of pseudo-emissivity and grain size of fragments was emphatically analyzed.

(1) The target pseudo-emissivity of the three rock chip specimens was basically consistent with the change law of their particle size after the normalization of the zenith angle fragment observation. When the fragment size is larger than 1 mm, the maximum pseudo-emissivity value appears in the fragment size of 5 mm, and when the fragment size is less than 1 mm, the pseudo-emissivity of rock fragments increases with the decrease in fragment sizes.

(2) Compared with the 1 mm particle size, the 5 mm particle size of the rock chip sample still has more flat surfaces, and the specular reflection of the flat surface leads to its radiation enhancement, and the calculated value of rock chip pseudo-emissivity increases. If the fragment size is increased between 1 and 5 mm, the trend of the particle size pseudo-emissivity curve should not change, but the extreme value may be shifted, and further detailed test exploration can be carried out later.

The basic law that the pseudo-emissivity of rock target changes with fragment size revealed in this study enriches and perfects the connotation of remote sensing rock mechanics and can provide a more rigorous experimental basis and analysis basis for thermal infrared remote sensing monitoring and data analysis of solid earth disasters, mine disasters, etc., such as remote identification of rock bulky falling caused by slope landslides disasters, etc. Future studies on loose-slope landslides are necessary to identify debris flows.

Author Contributions: Conceptualization, X.L., L.W., W.M. and L.S.; Methodology, L.W.; Validation, X.L., W.M. and L.S.; Writing—original draft, X.L.; Writing—review and editing, X.L., L.W., W.M., and L.S.; Supervision, L.W. All authors have read and agreed to the published version of the manuscript.

Funding: This work was supported by the State Key Program of the National Natural Science Foundation of China (Grant 41930108) and also by the Jiangxi Provincial Natural Science Foundation (Grant 20232ACB214007).

Data Availability Statement: Not available.

Conflicts of Interest: The authors declare no conflict of interest.

References

1. Wei, L.; Zhang, Y.; Zhao, Z.; Zhong, X.; Liu, S.; Mao, Y.; Li, J. Analysis of mining waste dump site stability based on multiple remote sensing technologies. *Remote Sens.* **2018**, *10*, 2025. [CrossRef]
2. Li, Q.M.; Yuan, H.N.; Zhong, M.H. Safety assessment of waste rock dump built on existing tailings ponds. *J. Cent. South Univ.* **2015**, *22*, 2707–2718. [CrossRef]
3. François, L. The mobility of long-runout landslides. *Eng. Geol.* **2002**, *3–4*, 301–331. [CrossRef]
4. Grechi, G.; Fiorucci, M.; Marmoni, G.M.; Martino, S. 3D thermal monitoring of jointed rock masses through infrared thermography and photogrammetry. *Remote Sens.* **2021**, *13*, 957. [CrossRef]
5. Chang, Z.; Du, Z.; Zhang, F.; Huang, F.; Chen, J.; Li, W.; Guo, Z. Landslide susceptibility prediction based on remote sensing images and GIS: Comparisons of supervised and unsupervised machine learning models. *Remote Sens.* **2020**, *12*, 502. [CrossRef]
6. Njoku, E.G.; Chan, S.K. Vegetation and surface roughness effects on AMSR-E land observations. *Remote Sens. Environ.* **2006**, *100*, 190–199. [CrossRef]
7. Mori, H.; Chen, X.; Leung, Y.F.; Shimokawa, D.; Man, K.L. Landslide hazard assessment by smoothed particle hydrodynamics with spatially variable soil properties and statistical rainfall distribution. *Can. Geotech. J.* **2020**, *57*, 1953–1969. [CrossRef]

8. Cuomo, S.; Moscariello, M.; Manzanal, D.; Pastor, M.; Foresta, V. Modelling the mechanical behaviour of a natural unsaturated pyroclastic soil within Generalized Plasticity framework. *Comput. Geotech.* **2018**, *99*, 191–202. [CrossRef]
9. Bao, Y.; Han, X.; Chen, J.; Zhang, W.; Zhan, J.; Sun, X.; Chen, M. Numerical assessment of failure potential of a large mine waste dump in Panzhihua City, China. *Eng. Geol.* **2019**, *253*, 171–183. [CrossRef]
10. Han, P.; Fan, X.; Tian, S.; Zhang, Y. Effect of Rainfall Intensity and Stone Content on the Instability of Quaternary Deposits. *Adv. Eng. Sci.* **2019**, *51*, 112–120. [CrossRef]
11. Cao, C.; Feng, J.; Tao, Z. Start-Up Mechanism and Dynamic Process of Landslides in the Full High Waste Dump. *Water* **2020**, *12*, 2543. [CrossRef]
12. Okada, Y.; Konishi, C. Geophysical features of shallow landslides induced by the 2015 Kanto-Tohoku heavy rain in Kanuma city, Tochigi Prefecture, Japan. *Landslides* **2019**, *16*, 2469–2483. [CrossRef]
13. Chen, G.; Li, H.; Wei, T.; Zhu, J. Searching for multistage sliding surfaces based on the discontinuous dynamic strength reduction method. *Eng. Geol.* **2021**, *286*, 106086. [CrossRef]
14. Cao, C.; Feng, J.; Tao, Z. 3D Numerical Simulation of Landslides for the Full High Waste Dump Using SPH Method. *Adv. Civ. Eng.* **2021**, *2021*, 1–16. [CrossRef]
15. Huang, K.; Xu, M.; Wang, Z. Experimental Study on Landslides of Loose Sediment Slope Induced by Stream Bed Incision. *Front. Earth Sci.* **2021**, *9*, 687358. [CrossRef]
16. Greco, R.; Comegna, L.; Damiano, E.; Marino, P.; Olivares, L.; Santonastaso, G.F. Recurrent rainfall-induced landslides on the slopes with pyroclastic cover of Partenio Mountains (Campania, Italy): Comparison of 1999 and 2019 events. *Eng. Geol.* **2021**, *288*, 106160. [CrossRef]
17. Chang, Z.; Huang, J.; Huang, F.; Bhuyan, K.; Meena, S.R.; Catani, F. Uncertainty analysis of non-landslide sample selection in landslide susceptibility prediction using slope unit-based machine learning models. *Gondwana Res.* **2023**, *117*, 307–320. [CrossRef]
18. Huang, F.; Xiong, H.; Yao, C.; Catani, F.; Zhou, C.; Huang, J. Uncertainties of landslide susceptibility prediction considering different landslide types. *J. Rock Mech. Geotech. Eng.* **2023**, *in press*. [CrossRef]
19. Liu, S.; Wu, L.; Mao, Y.; He, L.; Wang, Z.; Xu, Z.; Wei, L.; Yang, Z. Spaceborne-airborne-ground collaborated intelligent monitoring on open-pit slope and its typical applications. *J. China Coal Soc.* **2020**, *45*, 2265–2276.
20. Pappalardo, G.; Mineo, S. Investigation on the mechanical attitude of basaltic rocks from Mount Etna through infrared thermography and laboratory tests. *Constr. Build. Mater.* **2017**, *134*, 228–235. [CrossRef]
21. Liu, X.; Liang, Z.; Zhang, Y.; Liang, P.; Tian, B. Experimental study on the monitoring of rockburst in tunnels under dry and saturated conditions using ae and infrared monitoring. *Tunn. Undergr. Space Technol.* **2018**, *82*, 517–528. [CrossRef]
22. Xiao, F.; He, J.; Liu, Z.; Shen, Z.; Liu, G. Analysis on warning signs of damage of coal samples with different water contents and relevant damage evolution based on acoustic emission and infrared characterization. *Infrared Phys. Technol.* **2019**, *97*, 287–299. [CrossRef]
23. Christensen, P.R.; Bandfield, J.L.; Hamilton, V.E. A thermal emission spectral library of rock-forming minerals. *J. Geophys. Res.* **2000**, *105*, 9735–9739. [CrossRef]
24. Moersch, J.E.; Christensen, P.R. Thermal emission from particulate surfaces: A comparison of scattering models with measured spectra. *J. Geophys. Res.* **1995**, *100*, 7465–7477. [CrossRef]
25. Balick, L.; Gillespie, A.; French, A.; Danilina, I.; Allard, J.P.; Mushkin, A. Longwave thermal infrared spectral variability in individual rocks. *IEEE Geosci. Remote Sens. Lett.* **2009**, *6*, 52–56. [CrossRef]
26. Schlerf, M.; Rock, G.; Hecker, C.; Lagueux, P.; Udelhoven, T. A thermal infrared imaging spectrometer for natural resources applications—First results. In Proceedings of the 2013 5th Workshop on Hyperspectral Image and Signal Processing: Evolution in Remote Sensing (WHISPERS), Gainesville, FL, USA, 26–28 June 2013. [CrossRef]
27. Ramakrishnan, D.; Bharti, R.; Singh, K.D.; Nithya, M. Thermal inertia mapping and its application in mineral exploration: Results from mamandur polymetal prospect, India. *Geophys. J. Int.* **2013**, *195*, 357–368. [CrossRef]
28. Wu, L.; Liu, S.; Wu, Y.; Wang, C. Precursors for rock fracturing and failure—Part I: IRR image abnormalities. *Int. J. Rock Mech. Min. Sci.* **2006**, *43*, 473–482. [CrossRef]
29. Wu, L.; Liu, S.; Wu, Y.; Wang, C. Precursors for rock fracturing and failure—Part II: IRR T-curve abnormalities. *Int. J. Rock Mech. Min. Sci.* **2006**, *43*, 483–493. [CrossRef]
30. Liu, S.; Xu, Z.; Wei, J.; Huang, J.; Wu, L. Experimental study on microwave radiation from deforming and fracturing rock under loading outdoor. *IEEE Trans. Geosci. Remote Sens.* **2016**, *54*, 5578–5587. [CrossRef]
31. Huang, J.; Liu, S.; Gao, X.; Yang, Z.; Ni, Q.; Wu, L. Experimental Study of the Thermal Infrared Emissivity Variation of Loaded Rock and Its Significance. *Remote Sens.* **2018**, *6*, 818. [CrossRef]
32. Liu, X.; Wu, L.; Zhang, Y.; Mao, W. Localized Enhancement of Infrared Radiation Temperature of Rock Compressively Sheared to Fracturing Sliding: Features and Significance. *Front. Earth Sci.* **2021**, *9*, 756369. [CrossRef]
33. Zhan, W.; Chen, Y.; Ma, W.; Zhou, J.; Li, J. FOV effect analysis in directional brightness temperature observations for urban targets. *J. Remote Sens.* **2010**, *14*, 372–386. [CrossRef]
34. Adachi, Y.; Kikuchi, R.; Obata, K.; Yoshioka, H. Relative Azimuthal-Angle Matching (RAM): A Screening Method for GEO-LEO Reflectance Comparison in Middle Latitude Forests. *Remote Sens.* **2019**, *11*, 1095. [CrossRef]
35. Li, Z.; Petitcoling, F.; Zhang, R. A physically based algorithm for land surface emissivity retrieval from combined mid-infrared and thermal infrared. *Sci. China Ser. E* **2000**, *43*, 23–33. [CrossRef]

36. Liu, X.; Wu, L.; Zhang, Y.; Mao, W.; Qi, Y. Changing of rock fragments equivalent emissivity and its impact on localized positive infrared brightness temperature as rock fractured. *IEEE Geosci. Remote Sens. Lett.* **2023**, *20*, 3000205. [CrossRef]
37. Peng, Q.; Liu, Q.; Liu, Q.; Li, J.; Fang, L. Kernel-driven model fitting of multi-angle thermal infrared brightness temperature and its application. *J. Infrared Millim. Waves* **2011**, *30*, 361–365+371. [CrossRef]
38. Norman, J.M.; Kustas, W.P.; Humes, K.S. Source approach for estimating soil and vegetation energy fluxes in observations of directional radiometric surface temperature. *Agric. For. Meteorol.* **1995**, *77*, 263–293. [CrossRef]
39. Chang, Z.; Huang, F.; Huang, J.; Jiang, S.; Liu, Y.; Meena, S.R.; Catani, F. An updating of landslide susceptibility prediction from the perspective of space and time. *Geosci. Front.* **2023**, *14*, 101619. [CrossRef]
40. Zeng, Q.; Zhang, L.; Davies, T.; Yuan, G.; Xue, X.; Wei, R.; Yin, Q.; Liao, L. Morphology and inner structure of Luanshibao rock avalanche in Litang, China and its implications for long-runout mechanisms. *Eng. Geol.* **2019**, *260*, 105216. [CrossRef]

Disclaimer/Publisher's Note: The statements, opinions and data contained in all publications are solely those of the individual author(s) and contributor(s) and not of MDPI and/or the editor(s). MDPI and/or the editor(s) disclaim responsibility for any injury to people or property resulting from any ideas, methods, instructions or products referred to in the content.